Vertical shears of horizontal winds in the lower thermosphere observed by ICON

Scott L. England[1], Christoph R. Englert[2], Brian J. Harding[3], Colin C. Triplett[3], Kenneth Marr[2], John M. Harlander[4], Gary R. Swenson[5], Astrid Maute[6], and Thomas J. Immel[3]

[1] Aerospace and Ocean Engineering, Virginia Polytechnic Institute and State University, Blacksburg, Virginia, United States

[2] U.S. Naval Research Laboratory, Washington DC, United States

[3] Space Sciences Laboratory, University of California Berkeley, Berkeley, California, United States

[4] Space Systems Research Corporation, Alexandria, Virginia, United States

[5] Department of Electrical and Computer Engineering, University of Illinois Urbana-Champaign, Urbana, Illinois, United States

[6] National Center for Atmospheric Research, Boulder, Colorado, United States

Corresponding author: Scott L. England (englands@vt.edu), Orcid: 0000-0001-5336-0040

Key points

1. Strong horizontal wind shears with spatial scales from 100s km to over 10,000 km are observed with ICON MIGHTI

2. Systematic patterns in the strongest shears observed in the lower thermosphere are examined
3. The strongest shears display an altitude variation in local time that reflects the downward phase progression in the tidal winds

Abstract

Vertical shears of horizontal winds play an important role in the dynamics of the middle and upper atmosphere. Prior observations have indicated that these shears predominantly occur in the lower thermosphere. MIGHTI observations from the Ionospheric Connection Explorer indicate that strong wind shears are a common feature of the lower thermosphere and vary greatly between orbits. This work focuses on these strong shears, and examines their occurrences, horizontal scales and underlying organization. No preferred wind shear direction is found. The shears that persist for a short horizontal extent are slightly larger in amplitude and more numerous than those that persist across large horizontal scales. The altitude at which the strongest shears occur often shows a downward progression with local time, following the climatological winds. Consistent with prior observations, the strongest shears are often seen just below the wind maximum, which follows the downward phase propagation consistent with upward propagating tides.

Plain Language Summary

Understanding wind patterns is a key component to understanding our atmosphere. Gradients in these winds, seen as regions where slow and fast moving air are in close proximity, or air

moving in opposite directions is in close proximity, can play especially important roles in atmospheric motion and mixing of the air. At altitudes near the edge of space, such gradients are known to be especially large. New observations from the Ionospheric Connection Explorer (ICON) spacecraft have shown that these gradients are often present in this region, but can vary greatly from one orbit of the spacecraft to the next. This work examines the characteristics of the gradients observed with ICON. The analysis presented shows the direction and magnitude of these gradients, at what time of day and what altitude they are observed. The altitude where the strongest gradients are observed is shown to change with time of day.

1 Introduction

Vertical shears of horizontal winds play an important role in a variety of dynamical processes in the middle and upper atmosphere. The presence of strong shears can significantly impact and even inhibit the upward propagation of atmospheric gravity waves (e.g., Fritts and Alexander, 2003). Shears in zonal winds are believed to play a central role in producing narrow layers of metal ions associated with Sporadic-E (e.g., Whitehead, 1961; Axford, 1963, Larsen *et al*., 2005). In regions of the middle and upper atmosphere where such shears become especially large, the atmosphere can become dynamically unstable, leading to the formation of Kelvin-Helmholtz instabilities (e.g., Li et al 2005). While climatologies of the winds (e.g., HWM; Drob *et al*., 2015) reveal only modest wind shears in the lower thermosphere, high vertical-resolution observations (e.g., Larsen, 2002) frequently reveal shears that are close to this instability threshold, which may have important implications for the neutral dynamics of this region,

63 resulting in modified vertical constituent and heat fluxes as well as dynamo processes
64 impacting the ionosphere.

65

66 Both horizontal winds and their shears are especially strong in the region of the lower
67 thermosphere where the background vertical temperature gradient turns positive
68 (approximately 100 – 120 km altitude). These strong winds and shears are evident in global
69 climatologies of the wind (e.g., McLandress *et* al., 1996, Shepherd *et al*., 2012), which highlight
70 local amplitude maxima of atmospheric tides at these altitudes. In addition to such
71 climatologies, strong winds and shears are especially notable in individual samples of the winds
72 in this region, where the shears have been seen to maximize in the 100 – 110 km altitude
73 region (Larsen, 2002). Using global temperature observations, Offerman *et al*., (2009)
74 demonstrated that atmospheric waves persistently increase in amplitude in this altitude range.
75 Therefore, it is not surprising that observations of the winds and wind shears in this region
76 frequently exhibit strong wave-like fluctuations at this altitude (e.g., Djuth *et al*., 2010; Hysell *et*
77 *al*., 2014).

78

79 Examination of wind-shears in the lower thermosphere over approximately 100 – 120 km
80 altitude is not possible from the majority of ground-based radar systems (e.g., Jacobi and Arras,
81 2019). Altitude-resolved horizontal wind observations, suitable for determining vertical shears,
82 can be made in this altitude range from ground-based systems such as incoherent scatter
83 radars (e.g., Djuth *et al.*, 2010; Hysell *et al*., 2014) and lidars (e.g., Gardner and Papen, 1995;
84 Fritts *et al*., 2004; Oppenheim *et al*., 2009; Yue *et al*., 2010). Both kinds of instruments provide

detailed information on the vertical shears and their temporal evolution, but only at a very limited number of locations. Remote observations of rocket trails have been used to investigate winds and shears extensively (e.g., Larsen, 2002 and references therein). These also provide high-resolution vertical sampling of the wind across this altitude range. Although such observations have been made from low to polar latitudes, each rocket launch provides only one or two vertical profiles; thus they provide little information on the temporal or horizontal variation in the shears observed. Using over 400 such rocket trails observations, Larsen (2002) demonstrated that the observed maximum wind shear most often occurs in the vicinity of the altitude of maximum wind amplitude. Larsen and Fesen (2009) further analyzed the original Larsen (2002) data-set identifying the altitude of the maximum wind to be 100-105 km, exceeding 100 ms^{-1} in over 28% of the samples. No other pattern to the shears in local time (LT) or season was evident.

In contrast to the high-vertical resolution sampling offered from rocket trail observations, limb-viewing interferometers can provide lower vertical-resolution profiles of the winds in this region, with the advantage of being able to provide global-scale characteristics of the winds and shears (e.g., Shepherd *et al*., 2012; Liu *et al*., 2018). The magnitude of the shears estimated from such lower resolution measurements tend to be lower than those from the other instruments listed above, but the studies such as Liu *et al*. (2018) have been able to demonstrate global-variations in the shears, noting that they tend to maximize at mid-latitudes. What is not known is if there are other patterns governing where strong shears occur, or if there is a clear relationship between the very strong shears that are seen in individual vertical

profiles and climatologies of the winds in this region. Are the wind shears identified in rocket and ground-based measurements coherent across a large horizontal region or not?

Here we use one year of wind observations from the Ionospheric Connection Explorer (ICON) spacecraft (Immel *et al*., 2018) to examine the wind shears in the lower thermosphere. We examine the altitude of the strongest shears observed and their correspondence to the background wind magnitudes. The distribution of wind shears is examined, along with the spatial coherence of the wind shear, as seen parallel to the spacecraft orbit track. This study focuses on the largest wind shears observed, rather than a climatology of the winds and the shears evident therein (e.g., Yamazaki *et al*., 2021). The correspondence between strong shears seen in individual profiles and the climatology of the winds is determined.

2 Data and Method

The ICON Michelson Interferometer for Global High-Resolution Thermospheric Imaging (ICON MIGHTI; Englert *et al*., 2017) instrument measures the line-of-sight Doppler shift of airglow emission from atomic oxygen. Using two nearly orthogonal measurements separated by ~7 minutes, a horizonal wind vector is retrieved from these data (Harding *et al*., 2017). Here we use version 04 of the derived horizontal vector winds. During the daytime, the 557.7 nm emission is observed from 90 – 180 km tangent altitude. A measurement of the winds is made every 30 seconds, or approximately every 250 km great circle distance during the day. In the lower thermosphere, the horizontal winds are retrieved on a fixed vertical grid with a grid size of ~2.9 km.

Figure 1 shows an example of the daytime zonal wind observations from five successive orbits in March 2020. The data are shown such that the horizontal axis indicates LT. In four of the five orbits shown, strong shears in the zonal wind are evident in the lower thermosphere. In the first two orbits, strong shears of nearly the same gradient appear to persist over a large span of LT (and correspondingly longitude), changing slightly in altitude with LT. This pattern does not appear to be fixed in LT and is different on each of the five consecutive orbits shown. On the final orbit, the wind shears seen are significantly weaker. From this kind of plot, no overarching patterns are apparent from one orbit to the next or one day to the next.

As the altitude of the wind shears seen in Figure 1 varies with location, it is more useful to compute the maximum wind shear observed at any one time and record its location, rather than find the wind shears at a fixed altitude. There are several obvious ways to determine the wind shear, and here we chose to find the maximum gradient using a forward-difference approach (qualitatively similar results are achieved by using a central-difference approach, with sometimes smaller wind gradients estimated with such a technique if a gradient is not constant over the entire range). Even using this approach, it is worth acknowledging that MIGHTI lacks the vertical resolution to see the kind of wind shears reported in some of the prior studies noted in Section 1. For each zonal or meridional wind profile, we first select all data in the altitude range 92.8 – 133.1 km, which tends to envelope the region where the maximum wind shears are found, both in MIGHTI and prior studies (see Section 1). If all datapoints in that range are of good quality (using the ICON_L22_Wind_Quality variable), the maximum absolute

gradient is recorded and registered to the altitude of the midpoint of the two corresponding wind samples. Figure 2a shows this for the zonal wind profiles corresponding to the first orbit shown in Figure 1. The maximum wind shears at each longitude are highlighted. For all profiles, the maximum shear magnitude, direction (positive east, north), altitude, LT, longitude, and latitude are recorded. Figure 2b shows the gradients found for this orbit. The positive and negative shears identified for this orbit are shown with the red and blue symbols. In some regions of the orbit the maximum shear remains of a constant sign for a significant fraction of the globe, whereas in others it changes between positive and negative rapidly. For each datapoint, the horizontal scale over which the sign of the shear remains constant is recorded (the great circle distance shown by the horizontal red and blue lines). This process is then repeated for all observed profiles during the first complete year of the ICON mission, 2020. It is worth noting that the typical precision of the wind measurements is 5 m/s, so the 1-sigma uncertainty on the computed shear (using 5 measurements, separated by 2.9 km) is ~12 m/s/km. Shears greater than this are thus statistically significant at the 1-sigma level.

To compare the wind shears observed by ICON MIGHTI to those simulated in a global scale model, output from the ionosphere-thermosphere extension of the Whole Atmosphere Community Climate Model (WACCM-X 2.0; Liu *et al*., 2018) is used. To match the conditions observed by ICON, the GEOS5 reanalysis is used to specify dynamics in the lower atmosphere. This simulation used a 1.9° latitude, 2.5° longitude grid that is comparable to the MIGHTI sample size. It is worth noting that this model uses parametrized gravity waves to capture the

173 impacts of these sub-grid-scale features. The output of this model was sampled at the same
174 locations and times as every datapoint in the MIGHTI dataset and processed in the same
175 manner as described above.
176
177 **3 Results**
178 This section first details the properties of the maximum wind shears by examining the first 90
179 days (approximately two precession cycles) of data from 2020. Variations throughout the whole
180 year are then shown.
181
182 Figure 3a and b show the distribution of the magnitudes of the maximum zonal and meridional
183 shears over the first 90 days of 2020. Both distributions are symmetric about zero, meaning
184 that no preference for a shear direction is seen. Both show modal values in the region of 20
185 m/s/km, with the meridional shears begin slightly larger than the zonal ones. Shears above 40
186 m/s/km are seen, but at a low occurrence rate. As expected, this is lower than the maximum
187 shears reported from rocket trail data (e.g. Larsen, 2002), which had a higher vertical
188 resolution. To identify any trend in the shears with the horizontal scale of constant shear
189 direction, the population is divided into two groups consisting of the shears associated with a
190 horizontal scale of less than 2000 km great circle (short) with those beyond 2000 km great circle
191 (long). No apparent change in the distribution is evident in either case, implying no dependence
192 on the magnitude of the shear observed with the horizontal scale of constant shear direction.
193 The shears simulated in the WACCM-X model show the same overall trend as those seen in
194 MIGHTI, but with a factor of 2 lower shear magnitude seen in both the zonal and meridional

195 shears. This is likely due to the coarse model resolution, and its inability to resolve small-scale
196 gravity waves (see Liu, 2017).
197
198 The distribution of the observed horizontal scales of constant maximum wind shear direction
199 are shown in Figure 3c and d for the zonal and meridional shears respectively. Here the
200 occurrence rate refers to the fraction of the total wind samples in that group. A large fraction of
201 the distribution lies below 2000 km great circle distance, but horizontal scales of up to 10,000
202 km are occasionally observed. To identify if the horizontal scale of the constant maximum wind
203 shear direction is manifestly different between those of small and large shear magnitude, the
204 population is divided into two groups, above and below 15 m/s/km (based on Figure 3a and b,
205 and comparable to the 10 m/s/km threshold used by Liu *et al*., 2018). The population with large
206 shear magnitude is similar to the whole population, whereas those with small magnitude reveal
207 slightly fewer occurrences at the smallest great circle distances, and an increase at the larger
208 scales (especially clear in the meridional shears). Finally, the distribution for the shears found in
209 the WACCM-X output are shown. These show a much flatter distribution, with many fewer
210 occurrences of smaller horizontal scale events and more of the longer horizontal scale than
211 those observed by MIGHTI under any of the selection criteria.
212
213 Figure 3e and f show the altitude where the maximum wind shears occur. As seen in Figure 2
214 regions of both strong positive and negative shears can be seen within the same profile. Clear
215 patterns in the altitude of the maximum shears appear if only one shear direction is selected,
216 and here the negative meridional wind shears are shown. To further identify the pattern, only

217 shears in the 15 – 25° N latitude range are selected, and the data are shown as a function of
218 local time (LT). Figure 3e shows this for the entire population, whereas Figure 3f shows this only
219 for the short horizontal scale population described above. In both cases, a clear downward
220 progression of the altitude of maximum windshear is seen with increasing LT. In the case of the
221 latest LT bin, a new peak is evident at the very highest altitude, suggesting a cyclical pattern.
222 Looking at the rate of downward progression for example in panel e, the peak moves ~9 km
223 over 6 hours. If this represented a diurnal motion that would correspond to a 36 km in 24 hours
224 and for a semi-diurnal motion it would be 18 km in 12 hours. The diurnal motion would be
225 consistent with the wavelength of the migrating diurnal tide in this region (e.g., McLandress *et*
226 al., 1996; Akmaev *et al*., 1997). This behavior is investigated in more detail across the entire
227 year in Figure 4.
228
229 Figure 4 shows the altitude of the peak positive and negative wind shears in the 15 – 25° N
230 latitude throughout the whole year. Data are shown in 90-day increments, which provides
231 enough samples for notable patterns to be discerned in most cases. As in Figure 3e, each panel
232 shows the distribution of altitudes at three different LT ranges. The overall behavior noted in
233 Figure 3 of the descending altitude of the mode of the distribution with increasing LT is seen in
234 several panels (specifically a, b, e, h and k). There is no clear distinction between the behavior
235 of the positive and negative shears that persists throughout the year. In the panels that do not
236 display the same overall pattern as noted in Figure 3, the most common pattern is a single
237 altitude that does not change with LT (e.g., panels d and g). Finally, the tendency for a

238 secondary peak to appear at the higher altitudes in the final LT bin is visible in panels a, b, e, j
239 and k.
240
241 Comparing the altitude of the peak wind shear to the median wind values as a function of
242 altitude (Figure 4 panels c, f, i and l) reveals a likely cause of the downward progression noted
243 above. This climatological view of the average wind does not reveal the strong shears that are
244 the focus of this study, but rather the average wind associated with the migrating tides (as all
245 longitudes are averaged together, non-migrating components are minimized). These median
246 winds show a similar downward descent in the wind pattern with increasing LT as expected for
247 upward propagating tides. Comparing the first two columns of Figure 4 to the median winds, it
248 is evident that in most cases the peak positive or negative wind shears tend to occur at or just
249 below the altitudes where the average wind shows a strong positive or negative magnitude,
250 suggesting that the background tidal field governs the altitude at which we tend to see the
251 strong wind shears.
252
253 **4 Discussion and Conclusions**
254 This study focuses on the strongest wind shears observed by ICON MIGHTI, rather than on the
255 climatological winds and their shears. These strongest shears are most commonly seen in the
256 100 – 120 km altitude region, in agreement with that reported from prior rocket trail
257 observations (Larsen, 2002) and spacecraft-based observations (Liu *et al*., 2018).
258

Examining the degree of symmetry in Figure 3a, b there appears to be no preferred direction for the strong wind shears magnitudes. The WACCM-X results show the same symmetry, but generally lower shears. As both of these involve averages across all dayside LT, any signature of atmospheric tides (evident in Figure 4) would average out and thus produce this apparent symmetry. The observed meridional shears are generally slightly stronger than the zonal ones, but only by a few m/s/km, which is not seen in the model. The origin of this difference in zonal and meridional shears is not known.

Examining the differences between the short horizontal scale wind shears and either the whole population or the long horizontal scale shears, we see very little difference. This is clear in Figure 3a, b and comparing e to f. This implies that the population of short horizontal scale wind shears is not impacted significantly by any spurious datapoints or other non-geophysical source. While the origin of these short-horizontal scale shears is not clear from this study alone, one possible geophysical source would be small horizontal-scale gravity waves (e.g. Liu, 2017). Panels c and d show that the small horizontal-scale shears tend to have larger magnitudes, which is again apparent in panels a and b where the long scale is has a slightly large occurrence rate near the peak of the distribution, whereas the short scale occurs slightly more often at the highest wind shear values. If the small-scale shears are interpreted as features such as gravity waves and the large-scale shears as planetary-scale waves such as tide, this would imply that the large-scale signature is virtually always present and the strongest shear in the lower thermosphere is only short in scale when the gravity wave or other feature exceeds the amplitude of that large-scale pattern.

Exploring the possible tidal or other global-scale wave origin of the large-scale shears, Figure 3e and f show the clear downward progression in the altitude of the peak windshear with LT, which matches the downward propagation of the mean (primarily tidal) winds in this region. This is broadly similar to the tidal influence in Richardson number identified in lidar observations (e.g. Li *et al*., 2005; Yue *et al*., 2010). The meridional shears from 15 – 20° north were selected as the migrating diurnal tide is known to be clear in the meridional winds in this region (e.g., McLandress *et* al., 1996, Shepherd *et al*., 2012). The estimated downward progression rate of 36 km over 24 hours is consistent with the downward phase propagation of the migrating diurnal tide (e.g., McLandress *et* al., 1996; Akmaev *et al*., 1997), although additional information such as nighttime observations across this region would be needed to determine this definitively. Comparing panels e and f, the same downward phase progression is seen in the small-scale shears as the whole population, which would be consistent with the interpretation of these as associated with gravity waves, whose maximum wind shears tend to occur when they reinforce the larger-scale tidal wind pattern that exists in this region. The horizontal scale of low frequency gravity waves (periods of hours) have horizontal scales (>500 km) that can be observed by ICON limb sampling method, such as those identified by Hu et al. (2002).

Perhaps the most consistent pattern in Figure 4 is that the altitude at which the strongest individual shears are generally seen is just below the respective peak in the climatological winds (i.e., positive shears below a northward wind and vice versa). This is suggestive that these are

303 manifestations of the same underlying pattern, rather than the shears being organized by some
304 other small-scale process. This is reinforced by the similarity between the short and long-length
305 scale shears shown in Figure 3e and f. The high magnitude wind and the shears seen on
306 individual orbits, which greatly exceed those of the climatological winds, may be the result of
307 superposition of the dominant migrating tides with other waves, such as nonmigrating tides,
308 planetary waves and larger-horizontal scale gravity waves that are apparent in limb
309 observations. Nonetheless, the underlying pattern appears to be governed by the tides, at least
310 at the latitudes examined here. As the amplitude of the tides increase so do the shears, up to
311 the location of the maximum tidal wind amplitude, generally in the 100 – 120 km altitude
312 region. Above this, the upward propagating tides begin to dissipate and the most common wind
313 and shear patterns transition to being dominated by *in situ* generated tides, which tend to have
314 much larger vertical wavelengths.
315
316 The comparison of the observed wind shears to those simulated by WACCM-X provides a useful
317 comparison to a model dataset that contains realistically simulated large-scale waves (lower
318 atmosphere forcing from a reanalysis), but which lacks resolved small-scale waves or other
319 features below several hundred km horizontal scale. Liu (2016) demonstrated that the WACCM-
320 X model produces far larger shears when run at a higher resolution. Thus, the underestimation
321 of the shears in the lower-resolution model simulation used here, compared to those observed
322 by MIGHTI, is likely a result of the model resolution (Figure 3a, b). The model does reproduce
323 the observed symmetry in the wind shear direction, suggesting no preferred direction for these
324 shears in the lower thermosphere. Figure 3c and d show a very different distribution of shear

lengths than those observed, whereby the observed increase in the occurrence rate of short horizontal scale wind shears is not reproduced in the model. This would again be consistent with an interpretation that these are indeed the result of spatially small structures such as gravity waves, and not the sampling provided by MIGHTI. The larger-scale wind shears, out to even 10,000 km great circle distance, are reproduced in the model again suggesting these are geophysical features, such as related to atmospheric tides or other planetary-scale waves that are known to be strong in this altitude region.

Acknowledgements

This analysis used version 04 of the Level 2.2 ICON-MIGHTI horizontal wind data, which are available from the ICON website (https://icon.ssl.berkeley.edu/Data) and NASA's Space Physics Data Facility (https://cdaweb.gsfc.nasa.gov/pub/data/icon/). The WACCM-X model output used in this work is available from the National Center for Atmospheric Research's Climate Data Gateway at https://doi.org/10.5065/rjgt-g951. ICON is supported by NASA's Explorers Program through contracts NNG12FA45C and NNG12FA42I and NASA Grant 80NSSC2. The National Center for Atmospheric Research is sponsored by the National Science Foundation. The authors acknowledge the support from the International Space Science Institute (ISSI) through the International Team "An Exploration of the Valley Region in the Low Latitude Ionosphere: Response to Forcing from Below and Above and Relevance to Space Weather."

References

Akmaev, R. A., Yudin, V. A., and Ortland, D. A.: SMLTM simulations of the diurnal tide: comparison with UARS observations, Ann. Geophys., 15, 1187–1197, https://doi.org/10.1007/s00585-997-1187-7, 1997.

Axford, W. (1963). The formation and vertical movement of dense ionized layers in the ionosphere due to neutral wind shears. Journal of Geophysical Research, 68(3), 769–779.

Drob, D. P., et al. (2015). An update to the Horizontal Wind Model (HWM): The quiet time thermosphere. *Earth and Space Science, 2*. doi:10.1002/2014EA000089

Djuth, F. T., L. D. Zhang, D. J. Livneh, I. Seker, S. M. Smith, M. P. Sulzer, J. D. Mathews, and R. L. Walterscheid (2010), Arecibo's thermospheric gravity waves and the case for an ocean source, J. Geophys. Res., 115, A08305, doi:10.1029/2009JA014799.

Englert, C.R., Harlander, J.M., Brown, C.M., Marr, K.D., Miller, I.J., Stump, J.E., Hancock, J., Peterson, J.Q., Kumler, J., Morrow, W.H., Mooney, T.A., Ellis, S., Mende, S.B., Harris, S.E., Stevens, M.H., Makela, J.J., Harding, B.J., and Immel, T.J., 2017. Michelson Interferometer for Global High-resolution Thermospheric Imaging (MIGHTI): instrument design and calibration. Space Science Reviews, 212(1-2), pp.553-584. DOI: 10.1007/s11214-017-0358-4

366 Fritts, D. C., and M. J. Alexander, Gravity wave dynamics and effects in the middle atmosphere,
367 *Rev. Geophys., 41*(1), 1003, doi:10.1029/2001RG000106, 2003.

368

369 Fritts, D. C., Williams, B. P., She, C. Y., Vance, J. D., Rapp, M., Lübken, F.-J., Müllemann,
370 A., Schmidlin, F. J., and Goldberg, R. A. (2004), Observations of extreme temperature and wind
371 gradients near the summer mesopause during the MaCWAVE/MIDAS rocket
372 campaign, *Geophys. Res. Lett.*, 31, L24S06, doi:10.1029/2003GL019389.

373

374 Gardner, C. S., and G. C. Papen (1995), Mesospheric Na wind/temperature lidar, Rev. Laser Eng.,
375 23, 131–134.

376

377 Harding, B. J., Makela, J. J., Englert, C. R., Marr, K. D., Harlander, J. M., England, S. L., and Immel,
378 T. J., (2017). The MIGHTI wind retrieval algorithm: description and verification. Space Science
379 Reviews, 212: 585. https://doi.org/10.1007/s11214-017-0359-3

380

381 Hysell, D. L., M. F. Larsen, and M. P. Sulzer (2014), High time and height resolution neutral wind
382 profile measurements across the mesosphere/lower thermosphere region using the Arecibo
383 incoherent scatter radar, *J. Geophys. Res. Space Physics*, *119*, 2345–2358,
384 doi:10.1002/2013JA019621.

385

386 Hu, X., A. Liu, C.S. Gardner, and G. R Swenson (2002) Characteristics of quasi-monochromatic
387 GWs observed with Na lidar in the mesopause region at Starfire Optical Range, NM, GRL, Vol
388 29., p 2169, doi:10.1029/2002GL014975
389
390 Immel, T.J., England, S.L., Mende, S. B. et al., (2018). The Ionospheric Connection Explorer
391 Mission: Mission Goals and Design, Space Science Reviews, 214: 13.
392 https://doi.org/10.1007/s11214-017-0449-2
393
394 Jacobi, C., & Arras, C. (2019). Tidal wind shear observed by meteor radar and comparison with
395 sporadic E occurrence rates based on GPS radio occultation observations. Advances in Radio
396 Science, 17(GHJ), 213–224.
397
398 Larsen, M.F., (2002), Winds and shears in the mesosphere and lower thermosphere: Results
399 from four decades of chemical release wind measurements. J. Geophys. Res. 107, A8, 1215,
400 doi:10.1029/2001JA000218
401
402 Larsen, M. F., Yamamoto, M., Fukao, S., Tsunoda, R. T., & Saito, A. (2005). Observations of
403 neutral winds, wind shears, and wave structure during a sporadic-E/QP event.
404 Annales Geophysicae, 23(7), 2369–2375. https://doi.org/10.5194/angeo-23-2369-2005
405

406 Larsen, M. F. and C. Fesen, (2009), Accuracy issues of the existing thermospheric wind models:
407 can we rely on them in seeking solutions to wind-driven problems?, Ann. Geophys., vol 27, pp
408 2277-2284.
409
410 Li, F., A. Z. Liu, G. R. Swenson, J. H. Hecht, and W. A. Robinson (2005), Observations of gravity
411 wave breakdown into ripples associated with dynamical instabilities, J. Geophys. Res., 110,
412 D09S11, doi:10.1029/2004JD004849.
413
414 Liu, H.-L., Bardeen, C. G., Foster, B. T., Lauritzen, P., Liu, J., Lu, G., ... Wang, W. (2018).
415 Development and validation of the Whole Atmosphere Community Climate Model with
416 thermosphere and ionosphere extension (WACCM-X 2.0). Journal of Advances in Modeling
417 Earth Systems, 10. https://doi.org/10.1002/2017MS001232
418
419 Liu, H.-L. (2016), Variability and predictability of the space environment as related to lower
420 atmosphere forcing, *Space Weather*, *14*, 634–658, doi:10.1002/2016SW001450
421
422 Liu, H.-L. (2017). Large wind shears and their implications for diffusion in regions with enhanced
423 static stability: The mesopause and the tropopause. *Journal of Geophysical Research:*
424 *Atmospheres*, *122*, 9579–9590, https://doi.org/10.1002/ 2017JD026748
425

426 Liu, Y., Zhou, C., Tang, Q., Li, Z. Q., Song, Y., Qing, H. Y., Ni, B. B., and Zhao, Z. Y. (2018). The
427 seasonal distribution of sporadic E layers observed from radio occultation measurements and
428 its relation with wind shear measured by TIMED/TIDI. *Adv. Space Res.*, *62*(2), 426–
429 439. https://doi.org/10.1016/j.asr.2018.04.026
430
431 McLandress, C., Shepherd, G. G., and Solheim, B. H. (1996), Satellite observations of
432 thermospheric tides: Results from the Wind Imaging Interferometer on UARS, *J. Geophys.*
433 *Res.*, 101(D2), 4093– 4114, doi:10.1029/95JD03359.
434
435 Offermann, D., O. Gusev, M. Donner, J. M. Forbes, M. Hagan, M. G. Mlynczak, J. Oberheide, P.
436 Preusse, H. Schmidt, and J. M. Russell III (2009), Relative intensities of middle atmosphere
437 waves, J. Geophys. Res., 114, D06110, doi:10.1029/2008JD010662.
438
439 Oppenheim, M. M., Sugar, G., Slowey, N. O., Bass, E., Chau, J. L., and Close, S. (2009), Remote
440 sensing lower thermosphere wind profiles using non-specular meteor echoes, *Geophys. Res.*
441 *Lett.*, 36, L09817, doi:10.1029/2009GL037353.
442
443 Shepherd, G. G., et al. (2012), The Wind Imaging Interferometer (WINDII) on the Upper
444 Atmosphere Research Satellite: A 20 year perspective, Rev. Geophys., 50, RG2007,
445 doi:10.1029/2012RG000390.
446

Whitehead, J. (1961). The formation of the sporadic-E layer in the temperate zones. Journal of Atmospheric and Terrestrial Physics, 20(1), 49–58.

Yamazaki, Y., Arras, C., Andoh, S., Miyoshi, Y., Shinagawa, H., Harding, B. J., et al. (2022). Examining the wind shear theory of sporadic E with ICON/ MIGHTI winds and COSMIC-2 Radio 2 occultation data. *Geophysical Research Letters*, *49*, e2021GL096202. https://doi.org/10.1029/2021GL096202

Yue, J., She, C. -Y., & Liu, H. -L. (2010). Large wind shears and stabilities in the mesopause region observed by Na lidar at midlatitude. *Journal Of Geophysical Research-Space Physics*, *115*, A10307. doi:10.1029/2009JA014864

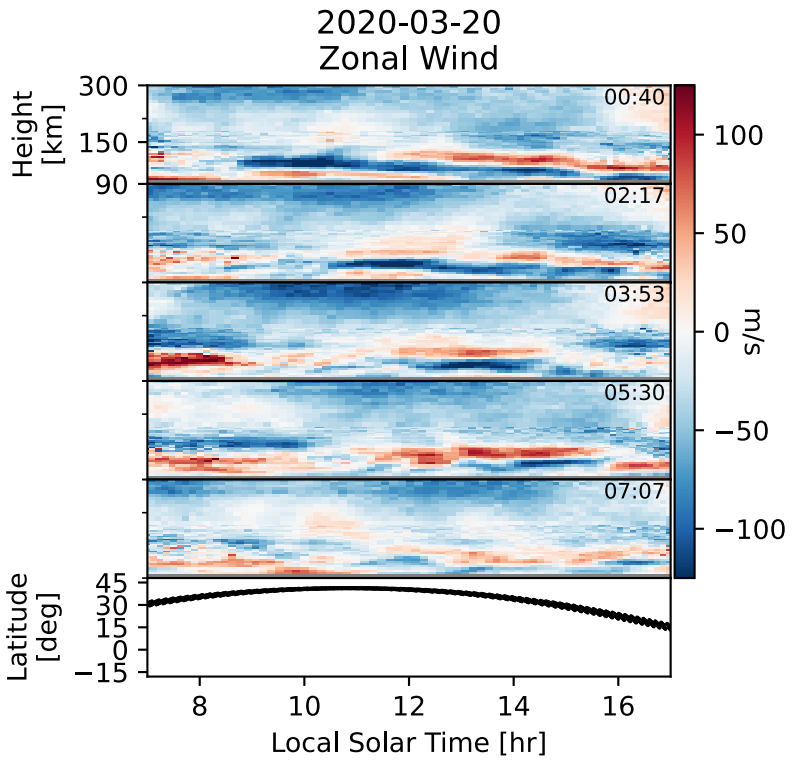

459

460 *Figure 1 – Daytime zonal winds observed with ICON MIGHTI on five successive orbits from*

461 *March 20th, 2020. Values are shown as functions of altitude and local time. The latitude of the*

462 *wind observations at 90 km altitude is shown in the bottom panel. The time at the middle of*

463 *each dayside orbit segment in UTC is noted. Strong wind shears can be seen in the lower altitude*

464 *region of each panel, with no obvious pattern repeating from one orbit to the next.*

465

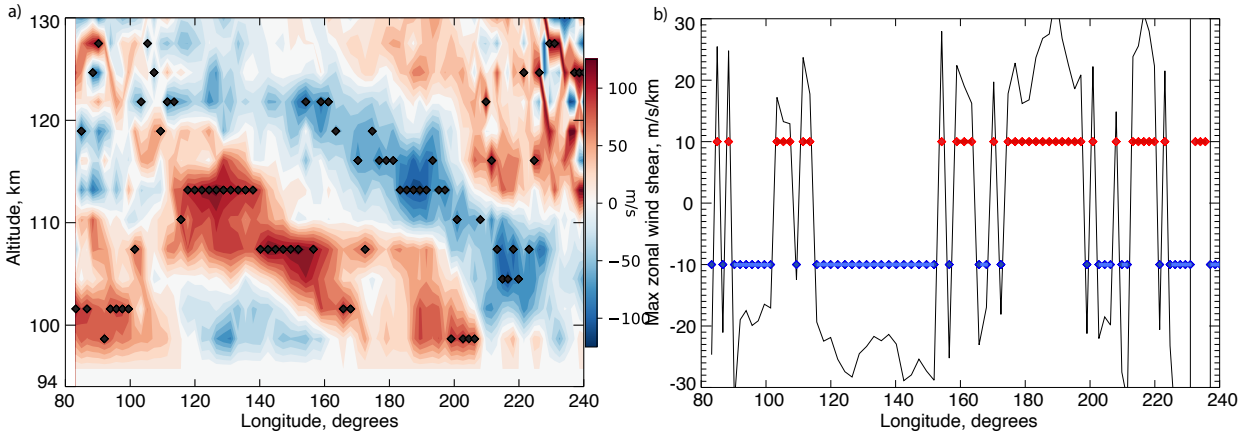

Figure 2 – Determination of the maximum wind shear and the horizontal scale of the direction of the wind shear. Panel a shows the daytime zonal wind profiles observed on the first orbit shown in Figure 1. The location of the maximum wind shear identified at each longitude is marked with diamonds. Panel b shows the maximum daytime zonal wind shears for the same orbit as panel a. The red and blue lines mark the portions of the orbit in which the shear is positive (becoming more eastwards with altitude) and negative, respectively.

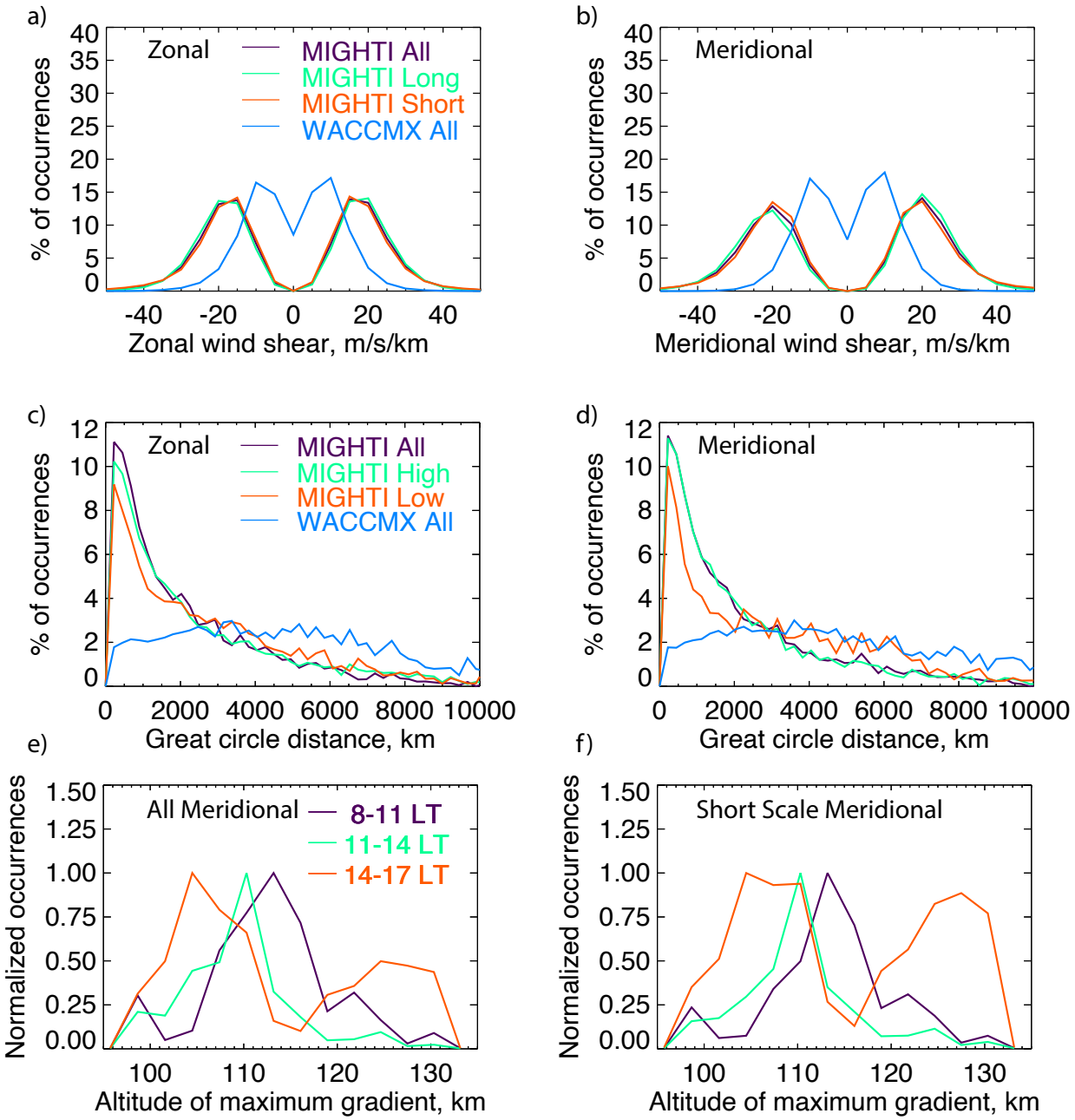

Figure 3 – Histograms of the daytime wind shears observed by ICON MIGHTI and simulated by WACCM-X for days 1 – 90 of 2020. Panels a and b show the fraction of wind zonal and meridional shears with direction and amplitude. The color-coding indicates the observed wind shears from the whole dataset, and those associated with long horizontal scale and short horizontal scale constant wind shear directions, where 2000 km great circle separates long from

short. Panels c and d show the fraction of zonal and meridional wind shears with the great circle horizontal scale of constant wind shear direction. The color-coding shows indicates the whole dataset, and those where the wind shears are low or high in magnitude, where low refers to <|15 m/s/km| and high is >|15 m/s/km|. Panels e and f show the altitude of the maximum meridional wind shear observed between 15 – 25 °N latitude. The color-coding shows the local time of the observation. Panel e is for negative meridional wind shears and panel f is for the short horizontal scale negative meridional shears. All values have been normalized against the maximum for clarity.

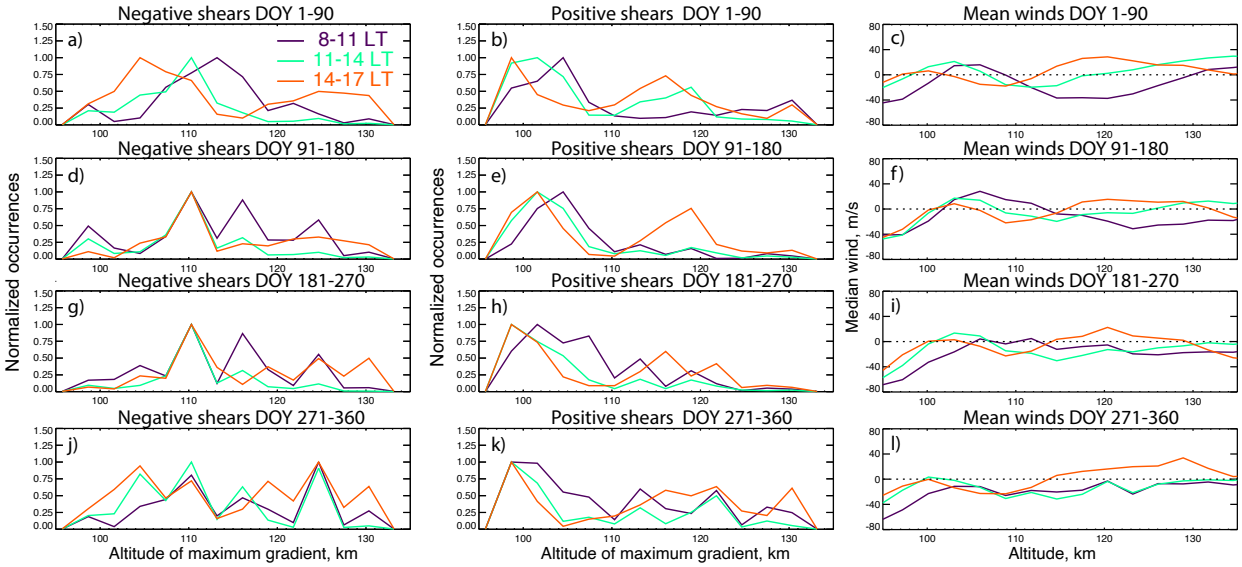

Figure 4 – Altitude of the maximum wind shear throughout 2020. Each pair of panels follows panels e from Figure 3. Panels a and b show days 1 – 90. Panels d and e show days 91 – 180. Panels g and h show days 181 – 270. Panels j and k show days 271 – 360. Panels a, d, g and j show negative shears and panels b, e, h and k show positive shears. Panels c, f, I and l show the median meridional winds as a function of height throughout the year. The dotted line marks zero.